Flood Monitoring by Integrating Normalized Difference Flood Index and Probability Distribution of Water Bodies

Fuqiang Xue, Wei Gao, Chao Yin, Xinyu Chen, Zhihong Xia, Yunzhe Lv, Yangyang Zhou, and Mengmeng Wang

***Abstract*—Climate change has caused an increase in the frequency of flood events. Rapid and accurate flood mapping is essential for disaster monitoring and risk assessment. The normalized difference flood index (NDFI) is a change detection method with the characteristics of efficient processing and less manual intervention, which can quickly obtain flood information. However, the NDFI method would misclassify some permanent water bodies in lakes and rivers into floods. We presented a framework by combining NDFI calculated from synthetic aperture radar images and a summer permanent water bodies (SPWB) exclusion layer derived from optical remote sensing surface reflectance data, abbreviated as NDFI-SPWB. This framework was further verified by the flood event in the Yangtze river basin in July 2020. Results show that the NDFI-SPWB framework can increase the user accuracy by approximately 10% and the Kappa coefficient by approximately 0.08 compared with the original NDFI method, which verifies the feasibility and effectiveness of the proposed framework.**

***Index Terms*—Flood extraction, summer permanent water bodies (SPWB), water probability.**

I. Introduction

FLOOD, as one of the most common natural disasters in the world, seriously affects the stability of ecosystems and also causes great harm to the safety of people and property [1], [2]. Governments and organizations should take measures to reduce and avoid flood disasters. In the meantime, the assessment for disaster is the basis of rescue and security works. Hence, accurately and efficiently obtaining information on the disaster areas is the primary prerequisite for postdisaster rescue and evaluation.

Manuscript received February 18, 2022; revised April 19, 2022; accepted May 6, 2022. Date of publication May 20, 2022; date of current version June 2, 2022. This work was supported by the Science and Technology Development Fund of Hubei Meteorological Bureau under Grant 2021Z04. *(Corresponding author: Wei Gao.)*

Fuqiang Xue, Wei Gao, Chao Yin, Xinyu Chen, Yangyang Zhou, and Mengmeng Wang are with the School of Geography and Information Engineering, China University of Geosciences, Wuhan 430074, China (e-mail: 1202010856@cug.edu.cn; gaowei@cug.edu.cn; yinchao0817@gmail.com; 1201920656@cug.edu.cn; 1201920701@cug.edu.cn; wangmm@cug.edu.cn).

Zhihong Xia is with the Wuhan Regional Climate Center, Wuhan 430000, China (e-mail: xiazhihongwrcc@hotmail.com).

Yunzhe Lv is with the State Key Laboratory of Remote Sensing Science, Aerospace Information Research Institute, Chinese Academy of Sciences, Beijing 100101, China, and also with the University of Chinese Academy of Sciences, Beijing 101408, China (e-mail: lv_yunzhe@foxmail.com).

Digital Object Identifier 10.1109/JSTARS.2022.3176388

Generally, heavy rainfall causing flooding is usually accompanied by many clouds, which will prevent the traditional optical remote sensing sensors from observing the land surface information. However, synthetic aperture radar (SAR) images are currently widely used in disaster research under extreme weather conditions as they are not limited by light and weather conditions [3]. Various methods were introduced to obtain flood information by using SAR images [4], [5], such as supervised classification [6], [7], threshold segmentation [8], [9], and change detection [10], [11]. The supervised classification method requires a training set, including extracting the marked submerged areas or core water location and its corresponding pixels from the SAR data. However, the training set cannot be automated produced, and it has individual local dependencies. The training samples are not well represented because of spectral differences of the same category in the image, and thus, a well-trained classifier in one domain may not work well in another [6], [12]. However, threshold segmentation and change detection methods can solve the shortcomings of supervised methods. For threshold segmentation, the specular reflection characteristics of open water have driven many studies [13], [14] to determine the threshold. Pixels below the threshold are identified as water. Given the effect of the roughness of wind and the environmental heterogeneity caused by the satellite system parameters, the backscatter coefficient value of the pixel will change. In addition, the single threshold method that only relies on a single threshold for image segmentation may not be suitable for flood detection in large areas [15]. The change detection method refers to the technology that compares the backscattering intensity before and during the flood event to detect the pixel change [16]. Long *et al.* [17] combined the advantages of the change detection algorithm and the threshold segmentation. However, the effectiveness of this method remains strongly dependent on users [17]. Cian *et al.* [18] proposed the flood index method based on Long *et al.* [17], who calculated the backscattering coefficient values of the two sets of images, distinguished flood areas through a threshold, and then extracted flood areas [18], [19].

Although the current change detection methods can achieve good accuracy [20], [21], they can still be improved in terms of the detection of specific details of land surface objects. When a disaster occurs, the backscattering coefficient values [22] of

ground objects obtained by satellite sensors will be different from the normal situation. Moreover, the backscattering coefficient values of many ground objects are relatively close [23]. Therefore, only relying on those values for flood mapping will cause many errors inevitably [24]. To eliminate these errors, many scholars set low backscattering coefficient masks or exclusion layers [25]. For example, Hardy *et al.* [26] and Tsyganskaya *et al.* [24] used shuttle radar topography mission (SRTM), SRTM Water Body Data, and Global Urban Footprint as auxiliary data to exclude urban areas and permanent water bodies and combine machine learning and OSTU [27] methods for the cartography of vegetation inundation [26], [28]. However, this method requires a certain training dataset, and it is difficult to deal with missing data.

The normalized difference flood index (NDFI) [18] is essentially a change detection method [29], [30]. The NDFI has the advantages of less manual intervention and rapid flood mapping. Moreover, the NDFI divides flood areas according to the difference between the mean and the minimum value of the backscattering coefficient values of the pixels [31]. However, owing to the presence of wind and the heterogeneity of the environment caused by the parameters of the satellite system, some areas of rivers and lakes with the same change pattern as the disaster areas are mistakenly classified as floods.

In this case, we presented a framework by combining NDFI calculated from SAR images and a summer permanent water bodies (SPWB) exclusion layer derived from optical remote sensing surface reflectance data, hereinafter referred to as NDFI-SPWB. The main objectives of this article are as follows.

1) Construct an exclusion layer based on historical data to improve the shortcomings of single use of NDFI.
2) Verify the feasibility and effectiveness of the proposed framework.

II. Methodology

The proposed NDFI-SPWB framework consists of three steps. First, the NDFI method is used to initially extract flood information. Then, the water probability is comprehensively calculated to construct the SPWB exclusion layer. Finally, the NDFI results are combined with the SPWB exclusion layer to obtain flood information. Fig. 1 shows the method flow chart.

A. NDFI According to the Change Law of Pixel Backscattering Coefficient

First, SAR data execute processes, such as radiation correction, filter processing, terrain correction, and logarithmic scale conversion. After those images are preprocessed, the flood index will be calculated. NDFI is a multitime statistical analysis of two sets of SAR images. One set only containing images of a nonflood period is considered as [32], whereas the other includes both the reference and the flood images. This method separately calculates the average backscatter value of each pixel in the reference images and the minimum backscatter value of each pixel in the reference and the flood images. Then, the method uses two statistical data acquired after calculation to derive and generate NDFI, that is, the standardized difference between the

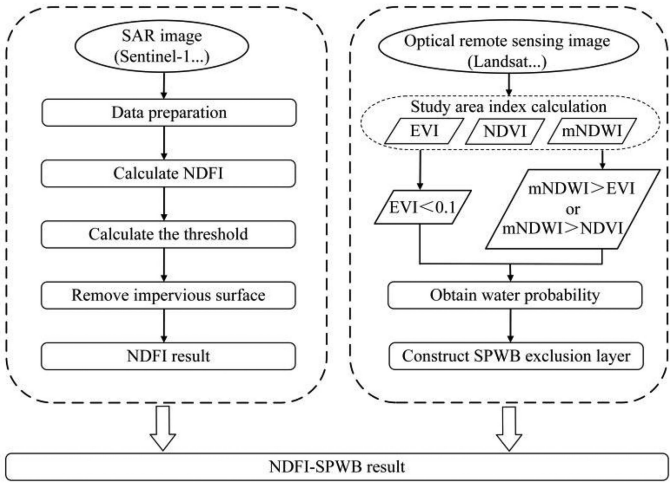

Fig. 1. Flowchart consists of three parts: firstly extract floods based on the NDFI method; then construct a SPWB exclusion layer based on historical data as a priori knowledge; finally extract floods based on the NDFI-SPWB framework.

mean (reference) and the minimum (reference + flood). The calculation formula is as follows:

$$\text{NDFI} = \frac{\text{mean}\sigma 0\ (\text{“reference”}) - \text{min}\sigma 0\ (\text{“reference + flood”})}{\text{mean}\sigma 0\ (\text{“}reference\text{”}) + \text{min}\sigma 0\ (\text{“reference + flood”})}. \tag{1}$$

Among them, mean *(“*reference*”)* represents the average backscatter coefficient of each pixel of the reference image, and min*(“*reference + flood*”)* refers to the minimum backscatter coefficient of each pixel of all images.

When calculating NDFI, the mean and min values of some picture elements are different, causing the NDFI to be much greater than 0 or less than -1. This result will affect the calculation of the NDFI threshold, and in turn affects the accuracy of the experimental results. Therefore, outliers, such as a picture element that is smaller than -1 or larger than 0, should be removed. After removing the outliers, the appropriate threshold for flood extraction could be determined more accurately. The threshold calculation formula is as follows:

$$th = \text{mean}\ (\text{NDFIflood}) - k * \text{std}\ (\text{NDFIflood}). \tag{2}$$

Among them, th represents the threshold, mean *(*NDFIflood*)* represents the average value of the entire difference image, and std *(*NDFIflood*)* stands for the standard deviation of the entire difference image. After the abnormal value is removed, a constant threshold is used to segment flood areas. Having conducted several case studies, Cian *et al.* [18] verified that $k = 1.5$ is the most effective value. The areas less than the threshold are flooded areas.

Owing to the unique imaging method of SAR satellites, buildings in urban areas have strong secondary bounce and multiple scattering effects. Hence, obtaining high-precision flood information in isolated flooded areas in cities and towns is difficult [24]. Therefore, urban areas should be eliminated based

on impervious surface data. Finally, the flood information is initially extracted.

B. Construct the Distribution Map of SPWB

The modified normalized difference water index (mNDWI) is one of the most widely used and the most effective methods to distinguish the characteristics of water body areas by using the normalized difference between the green band and the short-wave infrared band of remote sensing images [33], [34]. However, owing to the mixed distribution of aquatic plants in wetlands, mNDWI still has errors in distinguishing water bodies from vegetation [35]. Many studies showed that the combination of mNDWI, normalized difference vegetation index (NDVI) [36], [37], and enhanced vegetation index (EVI) [shown in formulas (3)—(5)] is much better and more stable than a single index in the mapping of flood [38]. The criteria of EVI below 0.1 can reduce the interference of wetland vegetation on wetland water extraction. We use the combination of mNDWI, NDVI, and EVI to extract water areas and combine the two standards of mNDWI $>$ NDVI and EVI $<$ 0.1, or mNDWI $>$ EVI and EVI $<$ 0.1 to identify surface water. Fig. 1 shows the method flow chart

$$\mathrm{NDVI} = \frac{\rho\mathrm{NIR} - \rho\mathrm{red}}{\rho\mathrm{NIR} + \rho\mathrm{red}} \tag{3}$$

$$m\mathrm{NDWI} = \frac{\rho\mathrm{green} - \rho\mathrm{SWIR1}}{\rho\mathrm{green} + \rho\mathrm{SWIR1}} \tag{4}$$

$$\mathrm{EVI} = 2.5 * \frac{\rho\mathrm{NIR} - \rho\mathrm{red}}{\rho\mathrm{NIR} + 6\rho\mathrm{red} - 7.5 * \rho\mathrm{blue} + 1}. \tag{5}$$

Among them, ρred, ρgreen, ρblue, ρNIR, and ρSWIR1 represent the reflectance of the red band, green band, blue band, short-wave infrared band, and the near-infrared band 1, respectively.

The pixels that meet the above standards will be classified as water bodies, and those that do not meet the standards will be regarded as nonwater bodies. We calculated the remote sensing indexes of 309 Landsat-8 images from June to August from 2013 to 2020 to identify the water bodies. After the probability of each pixel image of the water body is calculated, the probability map of the water body can be obtained. When the water probability is greater than 0.75, it would be noted as season permanent water bodies [39]. The final distribution map of SPWB is judged based on the probability of water bodies. This map is used to mask flood areas obtained by NDFI to eliminate the SPWB that are incorrectly classified as flood areas.

C. NDFI-SPWB Based on the Distribution of SPWB

Given that the applicability of NDFI in rivers and lakes needs to be improved, we presented a framework by combining NDFI calculated from SAR images and a SPWB exclusion layer derived from optical remote sensing surface reflectance data, abbreviated as NDFI-SPWB. This framework can give full play to the characteristics of the exclusion layer and retain the advantages of NDFI. It can also quickly and accurately conduct large-scale flood monitoring.

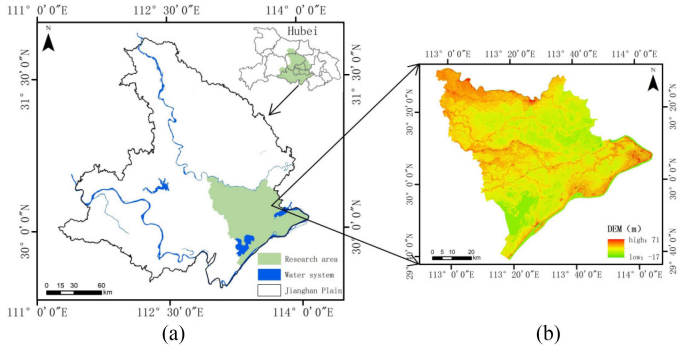

Fig. 2. Panel (a) shows the geographic location of the research area and panel (b) shows the corresponding elevation distribution map.

The NDFI-SPWB framework is mainly based on the SAR data using NDFI to initially extract flood damage in the study area and obtain the flood inundation area. Then, a series of steps will be performed to obtain the new flood inundation range, as shown in Fig. 1. Specifically, the water probability is detected by the combination of multiple remote sensing indexes to determine the range of the SPWB. Afterward, the SPWB exclusion layer is used as a mask to optimize the preliminary extraction results of the NDFI method.

III. Research Area and Data

A. Research Area

The "Extraordinary Heavy Rain and Flood Disasters in the Yangtze and Huaihe river Basins in July 2020" ranked first among the top 10 natural disasters in China in accordance with the Ministry of Emergency Management in 2020. According to statistics from the Hubei Meteorological Service,[1] from June 8 to July 17, 2020, the number of plum rainy days in Hubei Province has reached 39 days. Moreover, the cumulative average rainfall is 580 mm. Evident floods occurred in the Jianghan Plain, Hubei, China, and farmland was seriously damaged. In response to this flood event, the study selected the more severely affected areas of the Jianghan Plain as the research area, as shown in Fig. 2. Panel (a) shows the geographic location of the research area, and panel (b) depicts the corresponding elevation distribution map. The research area is located in the southeast of the Jianghan Plain, sandwiched between the Yangtze river and the Han river, with flat terrain and a subtropical monsoon climate. The spring and autumn are cloudy and rainy; the summer rainstorms are frequent, and floods can easily to happen. The main water areas involve the Yangtze river, Honghu lake, and Wu lake.

According to the flood event in the Yangtze river Basin in July 2020, we selected the images of July 13, 2020, and July 25, 2020, as the disaster images and July 1, 2020, as reference images for the research area.

B. Sentinel-1A GRD

The sentinel-1A GRD is an interferometric wide SAR carrying a C-band, which can provide long-term serial data. The data

[1] [Online]. Available: http://hb.cma.gov.cn/

can be obtained free of charge from the ESA website.[2] Given that co-polarized waves (HH/VV) are more effective in flood detection in non-submerged wetlands [40], [41], the image of the VV signal method is more sensitive to water body information. Thus, this article chooses the VV band for experiments.

In this article, sentinel-1 GRD data were preprocessed in the sentinel application platform (SNAP) software [42]. The preprocessing includes radiation calibration, filtering processing, terrain correction, and logarithmic scale conversion. In addition, SNAP software uses SRTM1 data to perform terrain correction on the filtered data, compensating for the errors caused by terrain changes and satellite sensor tilt [43]. GRD products have already undergone multiview and geocoding correction processing and no registration processing is required. The sentinel-1A GRD product is used to generate the flood inundation range.

C. Landsat-8 Surface Reflection Data

This article uses Landsat-8 standard grade 1T (L1T) terrain correction orthographic projection data on the Google Earth Engine (GEE) platform [44]. The correction coefficient is extracted from the image metadata, and the image resolution is 30 m. At present, GEE has been successfully used in the extraction of ground features information, such as urban land cover types, mangroves, crop planting areas, and open water bodies [45], [46]. Automatically running in parallel with fast computing allows GEE to deal with big data processing effectively [47]. The GEE platform [48], [49] uses the Landsat-8 Ecosystem Interference Adaptive Processing System algorithm for preprocessing [50].

The operational land imager carried out on Landsat-8 includes nine bands, and its band settings can meet the calculation of the comprehensive remote sensing indexes. This research, based on the GEE platform,[3] obtained all Landsat-8 surface images from 2013 to 2020. The Landsat-8 surface reflectance dataset is used to generate the SPWB exclusion layer.

D. SRTM1 Elevation Data

The elevation data selected for this article were jointly measured by NASA and the National Bureau of Surveying and Mapping of the Department of Defense in February 2000. The mission flew for 11 days, and its main goal was to map the terrain of the mainland. The elevation product used in this article is SRTM1, and the data can be obtained free of charge from the official website of the U.S. Geological Survey[4]. The dataset was opened to the world for free in 2014, and DEM products have been widely used in recent years. These elevation data are mainly used to generate slope data.

E. Land Cover Data

The land cover product data used in this article are the global 30-m fine land cover product (GLC_FCS30-2020) released by Zhang *et al.* [51]. The data can be obtained for free from the Earth Big Data Engineering Data Sharing Service Platform[5]. Founded on the 2015 global fine surface coverage product (GLC_FCS30-2015), this dataset is also combined with the 2019–2020 time-series Landsat surface reflectance data, Sentinel-1 SAR data, DEM terrain elevation data, global thematic auxiliary dataset and prior knowledge datasets and other refined surface covering products produced. Only the impervious surface category with a feature ID of 190 is extracted for eliminating urban areas in this article.

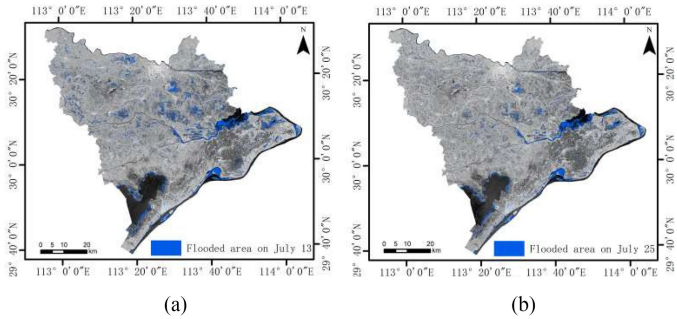

Fig. 3. Maps of flood damage based on NDFI: panel (a) shows flood areas on July 13; panel (b) shows flood areas on July 25.

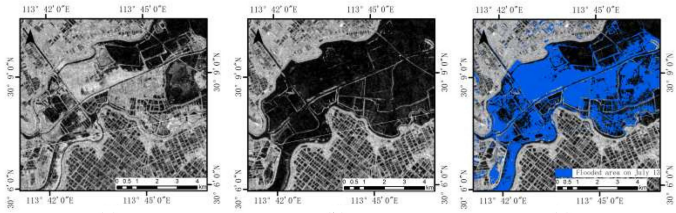

Fig. 4. Partial maps of the Wu Lake in the study area: panel (a) shows the Sentinel-1A GRD image on July 1, 2020; panel (b) shows the Sentinel-1A GRD image on July 13, 2020; panel (c) shows the flood damage information map extracted by NDFI.

IV. Result

A. Flood Information Extracted by NDFI

After preprocessing the sentinel-1A GRD products, the spatial distribution maps of the flood-affected areas are obtained, as shown in Fig. 3, where panels (a) and (b) show the flood damage maps of the research area on July 13 and 25, 2020, respectively. In the map, the blue areas indicate the affected areas. The flood areas are 241.20 and 189.20 km^2, respectively, showing a decreasing trend. The east and southwest parts of the study area are severely affected. Evidently, the affected areas are mainly around lakes and rivers. According to Fig. 2, the elevation changes of the study area are small, and the terrain is flat, so the error caused by mountain shadows can be ignored.

To intuitively demonstrate the flood extraction effect of NDFI, this article selects two typical areas of the Wu Lake and the farmland in the study area for analysis. Fig. 4 shows a partial map of the Wu Lake in the study area: panel (a) shows the Sentinel-1A

[2][Online]. Available: https://scihub.copernicus.eu/dhus/
[3][Online]. Available: https://earthengine.google.com
[4][Online]. Available: https://earthexplorer.usgs.gov/
[5][Online]. Available: http://data.casearth.cn/

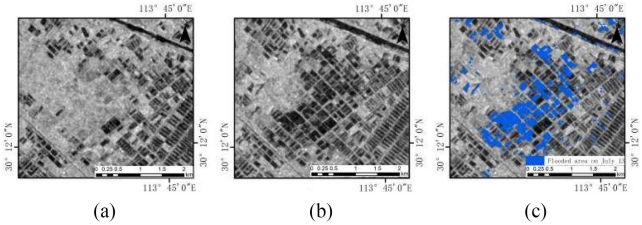

Fig. 5. Partial maps of the farmland in the study area: panel (a) shows the sentinel-1A GRD image on July 1, 2020; panel (b) shows the sentinel-1A GRD image on July 13, 2020; panel (c) shows the flood damage information map extracted by NDFI.

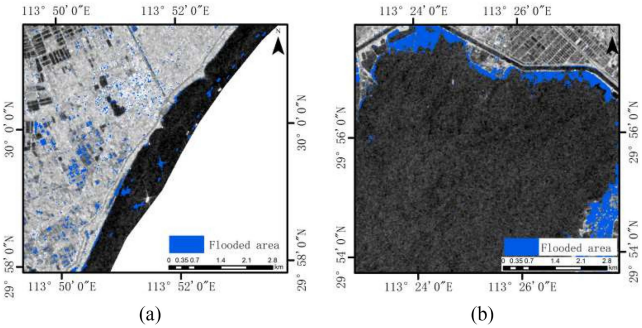

Fig. 6. Panel (a) shows the map of local flood damage in the Yangtze river; panel (b) shows the map of local flood damage in the Honghu lake.

GRD image on July 1, 2020, which is the image before the disaster; panel (b) presents the sentinel-1A GRD image on July 13, 2020, which is the image during the disaster; and panel (c) depicts the flood damage information map extracted by NDFI; the blue area indicates the affected areas. Under long-term heavy rainfall, the water level of the Wu Lake rises rapidly; the river channel is widened, floods are mainly concentrated on the south side of the river, and the texture is clear. In Fig. 5, panel (a) shows the image of the farmland area on July 1, 2020, which is the predisaster image; panel (b) presents the image of July 13, 2020, which is the disaster-affected image; panel (c) depicts the image extracted distribution map of farmland affected by disasters based on the NDFI method; the blue areas represent the affected areas. As the water levels of rivers and lakes in the Jianghan Plain are generally high, large areas of farmland are flooded. Therefore, the regular shape of the floods like farmland can be clearly seen in the images of the disaster. A comparison of sentinel-1A images before and during the disaster shows that NDFI has a good extraction effect.

Although NDFI has certain advantages in flood extraction, some shortcomings also exist. The following is a more intuitive display of the current problems of this method in river and lake areas. As shown in Fig. 6(a), the Yangtze river has many bright spots. In Fig. 6(b), some areas in the middle of the lake and the deep water in the lake are mistakenly divided into flood areas. In both cases, the backscattering coefficients of water bodies that are mistakenly divided into floods are much lower than normal water bodies. Therefore, they are misclassified as floods. Essentially, NDFI is a change detection algorithm, making this type of error inevitable.

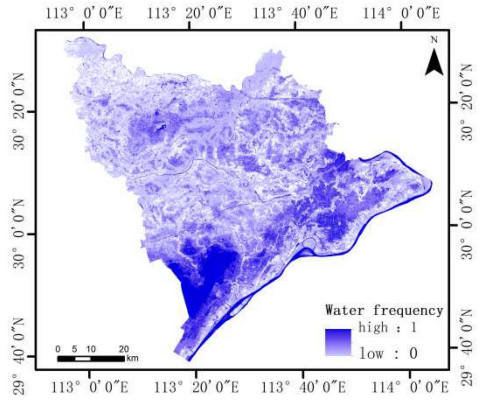

Fig. 7. Distribution map of water probability of the study area.

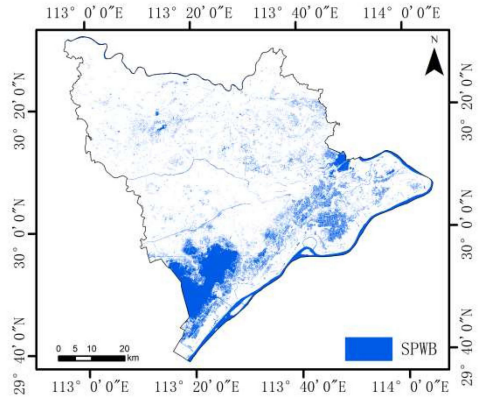

Fig. 8. Distribution map of SPWB of the study area.

B. Distribution Map of SPWB Based on Historical Data

After cloud removal processing of Landsat-8 images, those that meet the conditions are classified as water bodies. The distribution maps of water bodies in the study area are calculated in proper order. Then, all distribution maps of water bodies are superimposed to calculate the water probability. Fig. 7 shows the distribution map of the water probability of the study area.

When water probability is greater than 0.75, the pixel is classified as SPWB. Fig. 8 shows the distribution map of SPWB in the study area. The blue areas represent SPWB. SPWB is mainly located in the southern part of the study area because of the existence of "Honghu Lake" and close to the Yangtze river. This article finally uses the global 30-m fine surface cover product in 2020 as the verification data. The percentage of SPWB shown as water bodies and paddy fields in the dataset is 99.75%, and the percentage of incorrect division into other features is 0.25%.

C. Flood Information Extracted By NDFI-SPWB

In the article, the flood damage map in the rural areas is masked by an SPWB distribution map to obtain a new distribution map of flood damage. Fig. 9 shows the flood damage distribution maps of the NDFI-SPWB framework in the study area. The blue areas represent the inundated areas. We can see that the floods distribution of the NDFI-SPWB framework is

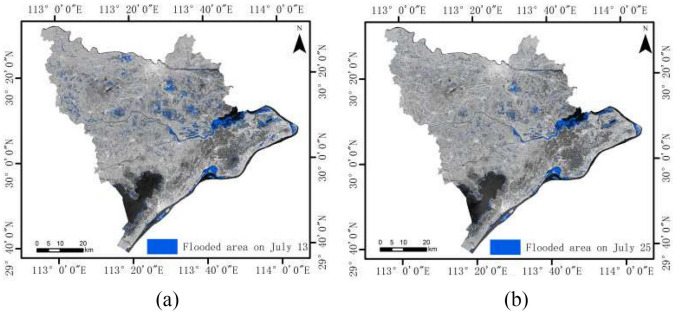

Fig. 9. Maps of flood damage based on NDFI-SPWB: panel (a) shows flood areas on July 13; panel (b) shows flood areas on July 25.

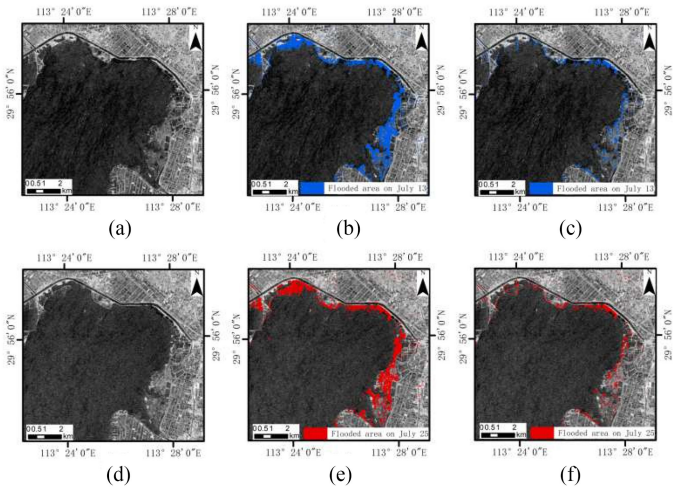

Fig. 10. Panels (a) and (d) show sentinel-1A GRD images on July 13 and July 25, respectively; panels (b) and (e) show the flood damage maps based on the preliminary extraction of NDFI on July 13 and July 25, respectively; panels (c) and (f) show the flood damage maps based on the extraction of NDFI-SPWB on July 13 and July 25, respectively.

mainly consistent with that of NDFI method. The floods in the study area are mainly located in the southwest and east. While, the flood areas calculated by NDFI-SPWB framework are 221.37 and 170.85 km^2, respectively, and the eliminated misclassification areas are 19.83 and 18.35 km^2, respectively.

There are some scenes where the NDFI-SPWB framework has outstanding performance in rural areas, namely, surrounding the lake and the river areas.

1) Lake Areas: In Fig. 10, panels (a) and (d) show Sentinel-1A GRD images on July 13 and July 25, respectively; panels (b) and (e) present the flood damage maps based on the preliminary extraction of NDFI on July 13 and July 25, respectively; panels (c) and (f) depict the flood damage maps based on the extraction of NDFI-SPWB on July 13 and July 25, respectively. The blue and red areas represent flooded areas. Fig. 10(b) and (e) shows that the lakeside is evidently submerged, whereas Fig. 10(c) and (f) shows the part of the inundation area that becomes less. Combined with the SPWB distribution map, areas that should be SPWB are misjudged as flood areas in panels (b) and (e). From panels (c) and (f), the NDFI-SPWB framework eliminates this part of the misjudgment.

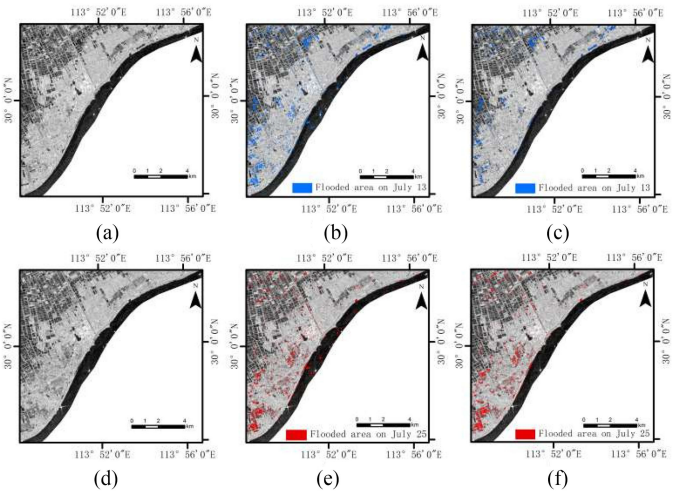

Fig. 11. Panels (a) and (d) show sentinel-1A GRD images on July 13 and July 25, respectively; panels (b) and (e) show the flood damage maps based on the preliminary extraction of NDFI on July 13 and July 25, respectively; panels (c) and (f) show the flood damage maps based on the extraction of NDFI-SPWB on July 13 and July 25, respectively.

TABLE I
ACCURACY EVALUATION RESULTS OF FLOOD EXTRACTION

Image date	Name	OA(%)	UA(%)	PA(%)	Kappa
07.13	NDFI	98.16	74.36	96.21	0.83
	NDFI-SPWB	98.60	83.32	96.21	0.91
07.25	NDFI	98.73	77.15	96.27	0.83
	NDFI-SPWB	99.21	87.89	96.27	0.91

2) River Areas: In Fig. 11, panels (a) and (d) present the base maps of sentinel 1A GRD images on July 13 and July 25, respectively; panels (b) and (e) show the flood damage maps initially extracted by NDFI on July 13 and July 25, respectively; panels (c) and (f) depict the flood damage maps extracted by NDFI-SPWB on July 13 and July 25, respectively. The blue and red areas represent flooded areas. Fig. 11(a) and (d) shows many bright areas and some normal water bodies in the middle of the Yangtze river, which are judged as flood areas in (b) and (e). Furthermore, panels (c) and (f) show that these errors are eliminated with the support of the SPWB exclusion layer.

D. Accuracy Evaluation

The accuracy verification method in this article uses the sentinel-2 images before and after the disaster; the sentinel-1A GRD images before and during the disaster; drone data; Google Maps; and the traditional single threshold method. The objectives are to obtain a visual interpretation of the flood map and decide the misclassification and omission of the article. This article chooses the confusion matrix to evaluate the accuracy and uses the producer accuracy (PA), user accuracy (UA), overall accuracy (OA), and Kappa coefficient to quantitatively describe the experimental results. From Table I, we can see that the OA is high, above 98%, and the Kappa coefficient is also above 0.8, indicating that the consistency of the confusion matrix is good. As no improvement in omission error (OE) is observed,

the PA should be the same for both names because OE and PA complement each other. Through the two groups of disaster imaging experiments, compared with the NDFI method, the OA of the NDFI-SPWB framework has been improved without loss of PA, the UA has increased by approximately 10%, and the Kappa coefficient has increased by approximately 0.08.

V. Discussion

A. Effectiveness Analysis of Water Body Probability for Eliminating Errors

The previous scene presentation part shows that the NDFI-SPWB framework has outstanding performance in lake and river areas. In the same scene, differences in the results of floods extracted by the NDFI method and the NDFI-SPWB framework are observed. The NDFI-SPWB framework is better and can solve the defect of the NDFI method.

In a flood event, using NDFI to extract floods has some shortcomings. Areas of lakes and rivers that should be normal water bodies are misjudged as floods. As shown in Fig. 6(a), ships of different sizes are distributed on the Yangtze river, reflecting the formation of bright spots of different sizes on the remote sensing images. Their existence increases the average backscattering coefficient of the area, increasing the difference from normal water bodies, in turn leading to misclassification of bright spots. According to Fig. 6(b), some areas in the middle of the lake and the deep water in the lake are mistakenly divided into flood areas. When a disaster occurs, under the influence of severe weather, the backscatter coefficient [22] of ground objects obtained by satellite sensors will be different from that outside of disasters. Therefore, the backscatter coefficient of water bodies that is misclassified as flood areas will be much larger than that of normal water bodies. The NDFI method divides flood areas according to the pattern of the backscatter coefficient of the pixel. Therefore, the ground features that follow the same pattern as pixels in these areas and disaster areas will be mistakenly classified as flood areas. The NDFI-SPWB framework can improve this shortcoming greatly. The biggest difference between the two is that the SPWB exclusion layer is constructed based on prior knowledge. Compared with the NDFI method, the accuracy of the result of the NDFI-SPWB framework has been greatly improved. With the support of the SPWB exclusion layer, the error in the misjudged flood areas is removed.

B. Effect of Different Season Permanent Water Bodies as Exclusion Layer on Framework

Fig. 12 shows the distribution maps of permanent water bodies in the four seasons of the year. From the figure, the most water bodies exist in winter, and the least water bodies are observed in summer. To show this difference more intuitively, Fig. 13 shows the distribution of permanent water bodies for 12 months. In winter, water bodies are most widely distributed in December, January, and February of the following year. In summer, water bodies are least widely distributed in June, July, and August. Combined with phenological analysis, this difference is because

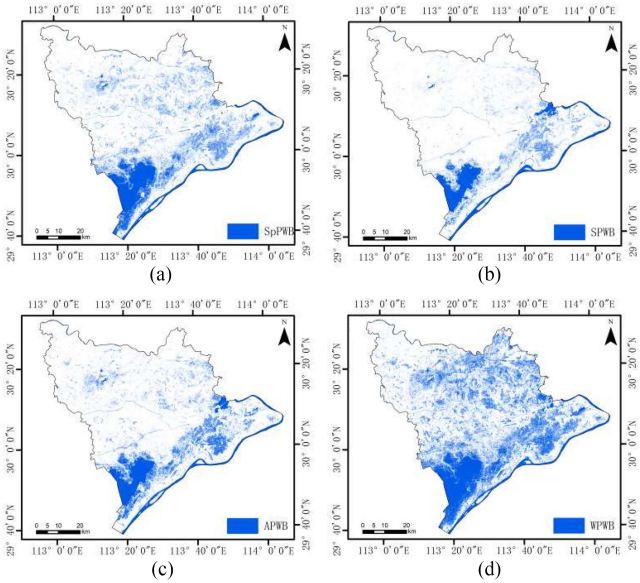

Fig. 12. Distribution maps of water bodies in four seasons (a) Map of spring permanent water bodies. (b) Map of SPWB. (c) Map of autumn permanent water bodies (APWB). (d) Map of winter permanent water bodies.

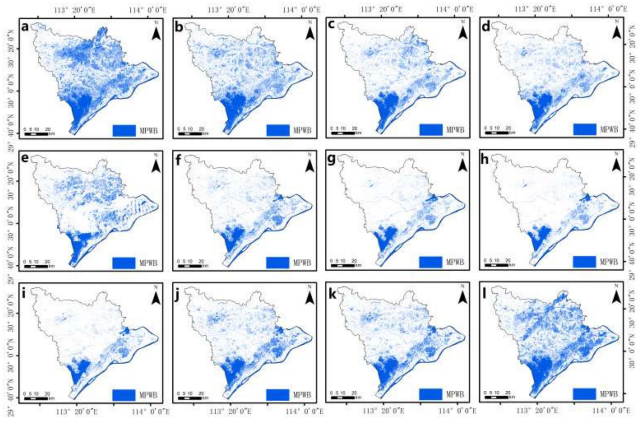

Fig. 13. Distribution maps of water bodies in 12 months: a-l represent the monthly permanent water bodies from January to December, respectively.

the study area is located in the Jianghan Plain where the rice-shrimp co-cropping model is different from the traditional rice planting model [52]. In this model, only one season of mid-season rice is planted, and the farmland is kept irrigated with a water depth of 50 cm for the rest of the time. The state of rice planting is in summer, whereas the state of water distribution is in winter. Compared with summer, the water area that increases in winter is the area of rice-shrimp co-cropping.

The exclusion layer used in the NDFI-SPWB framework is SPWB, and the time span is from June to August, rather than the annual permanent water body. When the annual water probability is greater than 0.75, it is regarded as a permanent water body; when the annual water probability is between 0.25 and 0.75, it is classified as a seasonal water body [53]. First, if the annual permanent water body is selected as the exclusion layer, then some rice-shrimp co-cropping areas will inevitably be misjudged as permanent water bodies, resulting in an increase in the area of the water body exclusion layer. This event will bring

errors to flood areas extracted by the NDFI-SPWB framework. The extracted flood areas will be smaller than the true value. Second, June to August is the flood season of the Yangtze river. This time period usually has more rainfall, and rivers and lakes are in the flood season. The time of flood event in the electoral districts occurs during the high water season, resulting in time overlap between the high water season and the flood period. When using NDFI to extract floods, the water of rivers and lakes during the high water season that changes every year should be SPWB, but it was misjudged as a flood. Therefore, when eliminating the misclassification error and selecting the exclusion layer, the SPWB should be selected. In this way, floods can be extracted quickly and accurately using the NDFI-SPWB framework.

For different flood disaster events, combined with the phenological data in the study area, annual permanent water bodies may be used as an exclusion layer to obtain more accurate flood information. In the face of different levels of flood disasters in different regions, whether the effectiveness of NDFI-SPWB framework will be influenced by different flood events needs to be considered, moreover, further rapid and accurate flood extraction needs to be researched in the future.

VI. Conclusion

The existing flood extraction methods cannot obtain flood information accurately, which can still be improved. To obtain flood information quickly and accurately, this article draws on the ideas of previous researchers and provides the NDFI-SPWB framework for obtaining disaster information of large-scale flooded areas based on sentinel-1A GRD images. First, the flood damage information of the disaster-stricken area in the study area is extracted through the NDFI method. Then, the remote sensing indexes are comprehensively calculated to obtain the water probability, then the SPWB exclusion layer is obtained. Finally, the SPWB pixels that are mistakenly divided into flood areas are removed.

We found that the NDFI-SPWB framework improves the mapping accuracy and reduces errors caused by the characteristics of the NDFI method. Compared with the NDFI method, the OA of the NDFI-SPWB framework has been improved without loss of PA, the UA has increased by approximately 10%, and the Kappa coefficient has increased by approximately 0.08. In addition, the NDFI-SPWB framework removes the summer permanent water pixels that are incorrectly classified as flood areas in lake and river areas. In this article, the NDFI-SPWB framework can be used in extreme weather conditions when historical data are used as prior knowledge. Furthermore, this framework can serve as an important tool to obtain more accurate coverage of flood disasters, perform rapid and large-scale flood mapping, and provide a scientific basis for efficient and high-precision disaster management and postdisaster assessment.

References

[1] S. Grimaldi, J. Xu, Y. Li, V. Pauwels, and J. P. Walker, "Flood mapping under vegetation using single SAR acquisitions," *Remote Sens. Environ.*, vol. 237, 2020, Art. no. 111582.

[2] M. Karamouz, Z. Zahmatkesh, and T. Saad, "Cloud computing in urban flood disaster management," in *Proc. World Environ. Water Resour. Congr.*, 2013, pp. 2747–2757.

[3] F. S. Marzano, S. Mori, J. A. Weinman, M. Montopoli, and R. Sensing, "Modeling polarimetric response of spaceborne synthetic aperture radar due to precipitating clouds from X- to Ka-band," *IEEE Trans. Geosci. Remote Sens.*, vol. 50, no. 3, pp. 687–703, Mar. 2012.

[4] D. E. Alsdorf, E. Rodríguez, and D. P. J. R. O. G. Lettenmaier, "Measuring surface water from space," *Rev. Geophys.*, vol. 45, no. 2, 2007, Art. no. RG2002.

[5] L. A. K. Mertes, "Remote sensing of riverine landscapes," *Freshwater Biol.*, vol. 47, no. 4, pp. 799–816, 2002.

[6] D. Borghys, Y. Yvinec, C. Perneel, A. Pizurica, and W. Philips, "Supervised feature-based classification of multi-channel SAR images," *Pattern Recognit. Lett.*, vol. 27, no. 4, pp. 252–258, 2006.

[7] S. Martinis, A. Twele, and S. Voigt, "Unsupervised extraction of flood-induced backscatter changes in SAR data using Markov image modeling on irregular graphs," *IEEE Trans. Geosci. Remote Sens.*, vol. 49, no. 1, pp. 251–263, Jan. 2011.

[8] Y. B. Dong, M. J. Li, and Y. Sun, "Research on threshold segmentation algorithms," *Adv. Mater. Res.*, vol. 860–863, pp. 2888–2891, 2013.

[9] S. Martinis and C. Rieke, "Backscatter analysis using multi-temporal and multi-frequency SAR data in the context of flood mapping at river Saale, Germany," *Remote Sens.*, vol. 7, no. 6, pp. 7732–7752, 2015.

[10] C. Stal, F. Tack, P. D. Maeyer, A. D. Wulf, and R. Goossens, "Airborne photogrammetry and Lidar for DSM extraction and 3D change detection over an urban area – A comparative study," *Int. J. Remote Sens.*, vol. 34, no. 4, pp. 1087–1110, 2013.

[11] X. Shen, E. N. Anagnostou, G. H. Allen, G. R. Brakenridge, and A. J. Kettner, "Near-real-time non-obstructed flood inundation mapping using synthetic aperture radar," *Remote Sens. Environ.*, vol. 221, pp. 302–315, 2019.

[12] S. S. Sreejamole and L. Ganesan, "Supervised classification of images using textural features," *Int. J. Soft Comput.*, vol. 4, no. 3, pp. 122–126, 2009.

[13] J. Lu *et al.*, "Automated flood detection with improved robustness and efficiency using multi-temporal SAR data," *Remote Sens. Lett.*, vol. 5, no. 3, pp. 240–248, 2014.

[14] D. Jie, M. Liao, X. Qiang, Z. Lu, M. Tang, and J. Gong, "Detection and displacement characterization of landslides using multi-temporal satellite SAR interferometry: A case study of Danba county in the Dadu river basin," *Eng. Geol.*, vol. 240, pp. 95–109, 2018.

[15] S. Martinis, A. Twele, and S. Voigt, "Towards operational near real-time flood detection using a split-based automatic thresholding procedure on high resolution TerraSAR-X data," *Nat. Hazards Earth Syst. Sci.*, vol. 9, no. 2, pp. 303–314, 2009.

[16] S. G. Dellepiane and E. Angiati, "A new method for cross-normalization and multitemporal visualization of SAR images for the detection of flooded areas," *IEEE Trans. Geosci. Remote Sens.*, vol. 50, no. 7, pp. 2765–2779, Jul. 2012.

[17] S. Long, L. E. Fatoyinbo, and F. Policelli, "Flood extent mapping for Namibia using change detection and thresholding with SAR," *Environ. Res. Lett.*, vol. 9, no. 3, pp. 206–222, 2014.

[18] F. Cian, M. Marconcini, and P. Ceccato, "Normalized difference flood index for rapid flood mapping: Taking advantage of EO Big Data," *Remote Sens. Environ.*, vol. 2019, pp. 712–730, 2018.

[19] F. Cian, M. Marconcini, P. Ceccato, and C. Giupponi, "Flood depth estimation by means of high-resolution SAR images and LiDAR data," *Nat. Hazards Earth Syst. Sci.*, vol. 18, no. 11, pp. 3063–3084, 2018.

[20] M. Souza Reis, L. V. Dutra, S. J. SiqueiraSant'Anna, and I. S. Escada, "Multi-source change detection with PALSAR data in the southern of pará state in the Brazilian Amazon – ScienceDirect," *Int. J. Appl. Earth Obs. Geoinf.*, vol. 84, 2020, Art. no. 101945.

[21] A. Asokan and J. Anitha, "Change detection techniques for remote sensing applications: A survey," *Earth Sci. Inf.*, vol. 12, pp. 143–160, 2019.

[22] X. Zhang, N. W. Chan, B. Pan, X. Ge, and H. Yang, "Mapping flood by the object-based method using backscattering coefficient and interference coherence of sentinel-1 time series," *Sci. Total Environ.*, vol. 794, 2021, Art. no. 148388.

[23] X. Lin, K. Wang, J. Wang, and X. Liu, "Realization of strong backscattering homogeneous regions with known backscattering coefficient in synthetic aperture radar images," *J. Appl. Remote Sens.*, vol. 11, no. 1, 2017, Art. no. 016018.

[24] V. Tsyganskaya, S. Martinis, P. Marzahn, and R. Ludwig, "Detection of temporary flooded vegetation using sentinel-1 time series data," *Remote Sens.*, vol. 10, no. 8, 2018, Art. no. 1286.

[25] S. Martinis, S. Plank, and K. Ćwik, "The use of sentinel-1 time-series data to improve flood monitoring in arid areas," *Remote Sens.*, vol. 10, no. 4, 2018, Art. no. 583.
[26] A. Hardy *et al.*, "Automatic detection of open and vegetated water bodies using sentinel 1 to map African malaria vector mosquito breeding habitats," *Remote Sens.*, vol. 11, no. 5, p. 593, 2019.
[27] Z. Dong, G. Wang, S. Amankwah, X. Wei, and A. Feng, "Monitoring the summer flooding in the Poyang lake area of China in 2020 based on sentinel-1 data and multiple convolutional neural networks," *Int. J. Appl. Earth Observ. Geoinf.*, vol. 102, no. 13, 2021, Art. no. 102400.
[28] N. Febrianti, F. Yulianto, M. Arda, and N. Haryani, "Flood inundation mapping using synthetic aperture radar data single polarization: A case study of flood in lake Tempe, South Sulawesi-Indonesia," in *Proc. IOP Conf. Ser., Earth Environ. Sci.*, vol. 572, 2020, Art. no. 012028.
[29] W. Cao, Z. Qiao, Z. Gao, S. Lu, and F. Tian, "Use of unmanned aerial vehicle imagery and a hybrid algorithm combining a watershed algorithm and adaptive threshold segmentation to extract wheat lodging," *Phys. Chem. Earth.*, vol. 123, 2021, Art. no. 103016.
[30] Y. Wang, "Otsu image threshold segmentation method based on seagull optimization algorithm," *J. Phys. Conf. Ser.*, vol. 1650, 2020, Art. no. 032181.
[31] J. Álvarez-Mozos *et al.*, "Correlation between ground measured soil moisture and RADARSAT-1 derived backscattering coefficient over an agricultural catchment of navarre (North of Spain)," *Biosyst. Eng.*, vol. 92, pp. 119–133, 2005.
[32] K. Jones, Y. Lanthier, P. der Voet, E. Valkengoed, D. Taylor, and D. Fernández-Prieto, "Monitoring and assessment of wetlands using earth observation: The Globwetland project - ScienceDirect," *J. Environ. Manage.*, vol. 90, no. 7, pp. 2154–2169, 2009.
[33] C. Verpoorter, T. Kutser, L. Tranvik, and O. Methods, "Automated mapping of water bodies using landsat multispectral data," *Limnol. Oceanogr. Methods*, vol. 10, no. 12, 2012.
[34] H. Xu, "Modification of normalised difference water index (NDWI) to enhance open water features in remotely sensed imagery," *Int. J. Remote Sens.*, vol. 27, no. 14, pp. 3025–3033, 2006.
[35] Z. Zou *et al.*, "Continued decrease of open surface water body area in oklahoma during 1984–2015," *Sci. Total Environ.*, vol. 595, pp. 451–460, 2017.
[36] A. Sh *et al.*, "Microphytobenthos spatio-temporal dynamics across an intertidal gradient using random forest classification and sentinel-2 imagery," *Sci. Total Environ.*, vol. 805, 2021, Art. no. 149983.
[37] C. Xu, X. Zhang, J. Zhang, Y. Chen, T. L. Yami, and Y. Hong, "Estimation of crop water requirement based on planting structure extraction from multi-temporal MODIS EVI," *Water Resour. Manage.*, vol. 35, pp. 2231–2247, 2021.
[38] X. Wang, X. Xiao, Z. Zou, B. Chen, and B. Li, "Tracking annual changes of coastal tidal flats in China during 1986–2016 through analyses of Landsat images with Google Earth Engine," *Remote Sens. Environ.*, vol. 238, 2018, Art. no. 110987.
[39] H. Xia, "Changes in water surface area during 1989–2017 in the huai river basin using Landsat data and Google Earth Engine," *Remote Sens.*, vol. 11, no. 15, 2019, Art. no. 1824.
[40] R. Westerhoff, M. P. H. Kleuskens, H. Winsemius, J. H. Huizinga, and R Brakenridge, "Automated and systematic water mapping in a near-real-time global flood observatory based on SAR data," *Hydrol. Earth Syst. Sci.*, vol. 17, pp. 651–663, 2012.
[41] A. Twele, W. Cao, S. Plank, and S. Martinis, "Sentinel-1-based flood mapping: A fully automated processing chain," *Int. J. Remote Sens.*, vol. 37, no. 13/14, pp. 2990–3004, 2016.
[42] D. Kpienbaareh, X. Sun, J. Wang, I. Luginaah, and L. Dakishoni, "Crop type and land cover mapping in northern Malawi using the integration of sentinel-1, sentinel-2, and planetscope satellite data," *Remote Sens.*, vol. 13, no. 4, 2021, Art. no. 700.
[43] S. B. Borah, T. Sivasankar, M. Ramya, and P. L. N. Raju, "Flood inundation mapping and monitoring in Kaziranga national park, Assam using sentinel-1 SAR data," *Environ. Monit. Assessment*, vol. 190, no. 9, pp. 520.1–520.11, 2018.
[44] R. Chen *et al.*, "Spatiotemporal continuous impervious surface mapping by fusion of Landsat time series data and Google Earth imagery," *Remote Sens.*, vol. 13, no. 12, 2021, Art. no. 2409.
[45] X. Jun *et al.*, "Nominal 30-m cropland extent map of continental Africa by integrating pixel-based and object-based algorithms using sentinel-2 and landsat-8 data on Google Earth Engine," *Remote Sens.*, vol. 9, no. 10, 2017, Art. no. 1065.
[46] X. Liu *et al.*, "High-resolution multi-temporal mapping of global urban land using Landsat images based on the Google Earth Engine platform," *Remote Sens. Environ.*, vol. 209, pp. 227–239, 2018.
[47] N. Gorelick, M. Hancher, M. Dixon, S. Ilyushchenko, and R. Moore, "Google earth engine: Planetary-scale geospatial analysis for everyone," *Remote Sens. Environ.*, vol. 202, pp. 18–27, 2017.
[48] C. Wang, M. Jia, N. Chen, and W. Wang, "Long-term surface water dynamics analysis based on Landsat imagery and the Google Earth Engine platform: A case study in the middle Yangtze River basin," *Remote Sens.*, vol. 10, no. 10, 2018, Art. no. 1635.
[49] Z. Zou, X. Xiao, J. Dong, Y. Qin, and J. Wang, "Divergent trends of open-surface water body area in the contiguous United States from 1984 to 2016," *PNAS*, vol. 115, no. 15, pp. 3810–3815, 2018.
[50] E. Vermote, C. Justice, M. Claverie, and B. Franch, "Preliminary analysis of the performance of the Landsat 8/OLI land surface reflectance product," *Remote Sens. Environ.*, vol. 185, pp. 46–56, 2016.
[51] X. Zhang, L. Liu, X. Chen, Y. Gao, and J. Mi, "GLC_FCS30: Global land-cover product with fine classification system at 30 m using time-series Landsat imagery," *Earth Syst. Sci. Data Discuss.*, vol. 2020, pp. 1–31, 2020.
[52] Y. I. Furong, T. Yang, Y. Zhao, Z. Tang, and F. Zhiqiang, "Effects of rice-shrimp co-cultivation on the nutrients in the topsoil layer of paddy field: Based on the empirical analysis of Nan County, Yiyang city," *Crop Res.*, vol. 33, pp. 424–427, 2019.
[53] H. Tian, N. Huang, Z. Niu, Y. Qin, J. Pei, and J. J. R. S. Wang, "Mapping winter crops in China with multi-source satellite imagery and phenology-based algorithm," *Remote Sens.*, vol. 11, no. 7, p. 820, 2019.

Fuqiang Xue received the B.S. degree in remote sensing science and technology from Anhui University of Science and Technology, Huainan, China, in 2020. He is currently working toward the M.S. degree in photogrammetry and remote sensing with the School of Geography and Information Engineering, China University of Geosciences, Wuhan, China. His major research interests include eco-environment remote sensing and monitoring, urban microclimate and the strategies to mitigate the urban heat island effect.

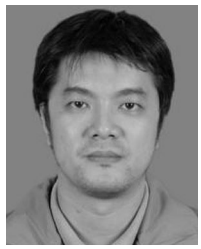

Wei Gao received the Ph.D. degree in cartography and geographical information engineering from China University of Geosciences, Wuhan, China, in 2010.

He is currently an Associate Professor with the School of Geography and Information Engineering, China University of Geosciences. His research interests include eco-environment and vegetation remote sensing and monitoring.

Chao Yin received the B.S. degree in remote sensing science and technology from Anhui University of Science and Technology, Huainan, China, in 2018, the M.S. degree in survey and mapping engineering from China University of Geosciences, Wuhan, China, in 2021.

His major research interests include eco-environment remote sensing and monitoring.

Xinyu Chen received the B.S. degree in survey and mapping engineering from Nanjing Tech University, Nanjing, China, in 2019. He is currently working toward the M.S. degree in survey and mapping engineering with the School of Geography and Information Engineering, China University of Geosciences, Wuhan, China.

His major research interests include consistency of multi-source remote sensing data and long time series surface water body monitoring.

Zhihong Xia received the Master of Engineering degree in Map Mapping and Geographic Information Engineering from China University of Geosciences, Wuhan, China, in 2006.

He is currently a Senior Engineer with the Wuhan Regional Climate Center. His main research interests include assessment of the impact of climate change on water resources and meteorological disaster risk assessment. Now, he presides over the project – "Study on Dynamic monitoring of multisource remote sensing rainstorm and flood disaster based on deep feature expression" of science and technology development fund from Hubei Meteorological Bureau.

Yunzhe Lv received the M.S. degree in photogrammetry and remote sensing from the China University of Geosciences, Wuhan, China, in 2020. He is currently working toward the Ph.D. degree with the State Key Laboratory of Remote Sensing Science, Aerospace Information Research Institute, Chinese Academy of Sciences, Beijing, China, University of Chinese Academy of Sciences, Beijing, China.

His major research interests include water cycle remote sensing.

Yangyang Zhou received the B.S. degree in geography information science from Anhui Normal University, Hefei, China, in 2019. She is currently working toward the M.S. degree in survey and mapping engineering with the School of Geography and Information Engineering, China University of Geosciences, Wuhan, China.

Her major research interests include urban microclimate and the strategies to mitigate the urban heat island effect.

Mengmeng Wang received the B.S. degree in geoscience information system from Hefei University of Technology, Hefei, China, in 2012, and the Ph.D. degree in photogrammetry and remote sensing from the Institute of Remote Sensing and Digital Earth, Chinese Academy of Sciences, Beijing, China, in 2017.

He is currently a Lecturer with the School of Geography and Information Engineering, China University of Geosciences, Wuhan, China. His main research interests include thermal infrared quantitative remote sensing and their applications on nature hazards and agriculture.